Periodic and Quasi-Periodic Orbits near Close Planetary Moons

Nicola Baresi, Lamberto Dell'Elce

Periodic and quasi-periodic orbits near close planetary moons

Nicola Baresi *
Surrey Space Centre, University of Surrey, Guildford, Surrey, GU2 7XH, UK

Lamberto Dell'Elce†
Inria Sophia Antipolis & Université Côte d'Azur, Sophia Antipolis, Valbonne, 06902 , France

Upcoming missions towards remote planetary moons will fly towards chaotic dynamical environments that are significantly perturbed by the oblateness of the host planet. This paper introduces a new time-periodic set of equations of motion that is based on the analytical solution of the zonal equatorial problem. Such a system, hereby referred to as the Zonal Hill Problem, remains populated by resonant periodic orbits and families of two-dimensional quasi-periodic invariant tori that are calculated by means of homotopy continuation procedures. The resulting periodic and quasi-periodic trajectories are investigated for the trajectory design of future planetary moons explorers.

I. Introduction

In the past few decades, there has been an increasing interest towards the deep-space exploration of planetary moons. Since the remarkable discoveries of the Cassini orbiter [1], both NASA and ESA have made plans to enhance our understanding of the Galilean moons of Jupiter. The Jupiter Icy Moons Explorer (JUICE) will be launching in 2023 with the goal of studying and better characterizing the subsurface oceans of Europa, Ganymede, and Callisto [2, 3]. The spacecraft will be joined in orbit around Jupiter by the NASA's Europa Clipper, which will dedicate most of its time in orbit around the gas giant to conduct a very high-resolution mapping of the icy moon [4]. The Martian Moons eXploration mission (MMX), which will attempt sample retrieval from the surface of Phobos, will also join the fleet of planetary moons' explorers in 2024 [5]. If successful, MMX will provide scientists with invaluable data on the origin and evolution of the Martian system, thus shading light on how water and other volatiles might have been delivered to Earth from the outer regions of the solar system [6].

In order to fulfill these ambitious scientific objectives, all of the proposed missions will have to operate in the vicinity of planetary moons and cope with strongly chaotic dynamical environments that are far from Earth. For instance, Phobos can be modelled as a giant potato-shaped like body that orbits just a few Mars-radii away from the surface of the Red planet [7]. Owing to the relatively short distances with respect to their corresponding host planet, the dynamics of a spacecraft near a planetary moon can be well approximated via the equations of the restricted three-body problem [8, 9].

*Lecturer, Surrey Space Centre, University of Surrey, n.baresi@surrey.ac.uk.
†Researcher, Inria Sophia Antipolis & Université Côte d'Azur.

However, work in the literature remain focused on the circular restricted three-body problem[10–12], without sufficient consideration for eccentricity and other time-varying effects that can significantly affect the dynamics of mass particles near planetary moons [13–16].

A major source of perturbation is the oblateness of the host planet. Such a source can not only affect the orbital evolutions of spacecraft and planetary moons [13], but also generate torques and libration angles that can provide a great deal of information regarding the internal mass distributions of the target object [17]. The tidal interaction between a moon and its host planet can also explain why the majority of the moons can be found near the equatorial regions (c.f., Fig. 5), an observation that can ultimately contribute to simplify the equations of motion of a spacecraft near these planetary objects and enable novel and higher-fidelity simulations for trajectory design approaches.

In this paper, we develop a new time-periodic set of equations of motion that is based on the analytical solution of the zonal equatorial problem [18, 19]. The dynamical model is hereby referred to as the Zonal Hill Problem (ZHP) and it remains populated by families of two-dimensional quasi-periodic invariant tori when the oblateness of the host planet is nonzero. An homotopy continuation procedure based on collocation [20] and the GMOS algorithm [21–24] is introduced so as to grow families of periodic orbits into their dynamical substitutes and explore applications of quasi-periodic trajectories for the mission analysis and design of planetary moons explorers. The resulting quasi-periodic trajectories, along with resonant periodic orbits that replace the L_1 and L_2 Lagrangian points along the planet and anti-planet directions, are complemented by stable and unstable manifolds emanating from hyperbolic solutions and offering new geometrical insight into the dynamical environment of planetary moon systems.

The paper is structured as follows: Section II overviews the analytical solution of the zonal equatorial problem to lay out the foundation for the derivation of the equations of motion of the ZHP (Section III). A numerical procedure is introduced in Section IV to calculate periodic and quasi-periodic solutions of this model, and to showcase trajectories in the Mars-Phobos, Jupiter-Io, and Saturn-Enceladus systems. Stable and unstable manifolds emanating from hyperbolic solutions are also briefly illustrated.

II. Analytical Solution of the Zonal Equatorial Problem

Consider the motion of a spherical moon (the secondary) subject to the gravitational attraction of an oblate host planet (the primary). The trajectory of the moon is better analyzed in an inertial reference frame centered on the host planet and such that $\hat{\boldsymbol{I}}$ is pointing towards a reference point (e.g., the vernal equinox for Earth or the periapsis of the moon's orbit at epoch), $\hat{\boldsymbol{K}}$ is perpendicular to the equatorial plane of the planet, and $\hat{\boldsymbol{J}} = \hat{\boldsymbol{K}} \times \hat{\boldsymbol{I}}$. Furthermore, the moon is assumed to be on an equatorial orbit such that its equations of motion may be described in polar coordinates (see Fig.

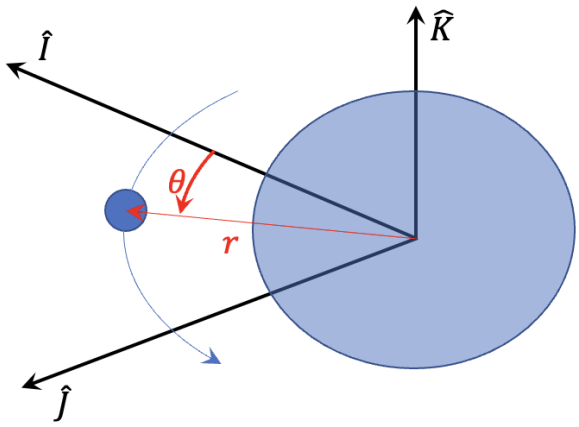

Fig. 1 Frames and Polar Coordinates definition for the analytical solution of the Zonal Equatorial Problem [18, 19].

1) [18]:

$$\ddot{r} - r\,\dot{\theta}^2 + \frac{\mu}{r^2} + \frac{J_0}{r^4} = 0, \tag{1a}$$

$$\ddot{\theta}\,r + 2\,\dot{\theta}\,\dot{r} = 0. \tag{1b}$$

In Eq. (1), r denotes the distance between the moon and the barycentre of the host planet, whereas θ represents the true longitude of the secondary in the equatorial plane of the primary. Moreover, μ is the gravitational parameter of the host planet, and $J_0 = \frac{3}{2}\,\mu\,J_2\,Re^2$ is a constant related to its second zonal harmonic coefficient and equatorial radius, respectively. Equation (1b) can be solved analytically by multiplying both terms for $\dot{r}$ and integrating on both sides. Similarly to the Two-Body Problem (TBP), the result proves that $H_0 = \dot{\theta}\,r^2$, namely the magnitude of the moon's specific orbital angular momentum, is an integral of motion.

Following Jezewski [18], one can substitute Eq. (1b) into (1a) in order to deduce an expression for a second integral of motion:

$$E = \frac{\dot{r}^2}{2} - \frac{\mu}{r} + \frac{H_0^2}{2\,r^2} - \frac{J_0}{3\,r^3}, \tag{2}$$

which is hereby referred to as the specific energy of the oblate equatorial two-body problem. By defining

$$\Phi_{eff} = -\frac{\mu}{r} + \frac{H_0^2}{2\,r^2} - \frac{J_0}{3\,r^3} \tag{3}$$

as the effective potential, Eq. (2) can be re-arranged to partition the equatorial plane of the host planet between areas of admissible motion and forbidden regions. The boundaries of these regions are zero-velocity curves $\mathcal{Z}(r) := \left\{\forall r \in \mathbb{R} | \Phi_{eff}(r, H_0, J_0) = E\right\}$.

Figure 2 illustrates the difference between the zero-velocity curves for the Mars-Phobos example, with and without the contributions due to Mars' oblateness: $J_2 = 1960.45 \times 10^{-6}$. The values of r are shown in Mars equatorial radii, with $R_e = 3389.5$ km and $\mu = 42828.3736$ km^3/s^2. As for the value of $H_0 = 20038.773568918$ km^2/s and $E = -2.28403589161379$ km^2/s^2, these are extracted from NASA's SPICE Phobos ephemerides [25, 26] after propagating over 100 orbital periods from Apr 25, 2025, 12:00:00 UTC. As it can be seen, the oblateness of red planet lowers the value of E, thereby affecting the periapsis and apoapsis altitudes of the Martian moon. Indeed, it is found that $E = -2.28403589161379$ km^2/s^2 intersects the effective potential in two points, representing the minimum and maximum distances from the surface of Mars. Note that in the plot, the value of $E = -0.1807$ is reported in normalized units, with R_e and $\sqrt{R_e^3/\mu}$ as the length and time units, respectively.

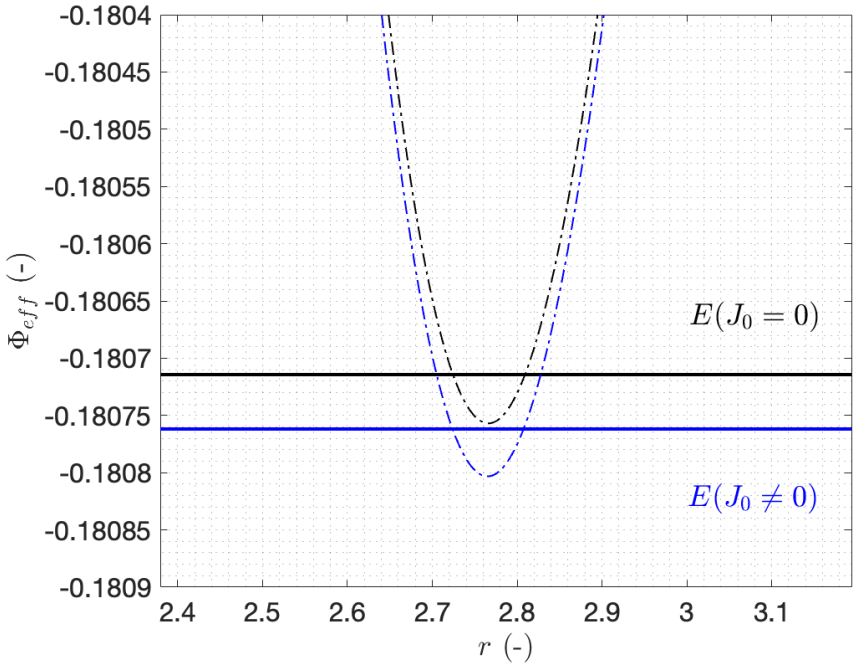

Fig. 2 Zero-Velocity "curves" for the Mars-Phobos example with and without J_2 effects. The distance values are shown in Mars equatorial radii $R_e = 3389.5$ km. Motion above the horizontal lines is forbidden.

The apsides of the secondary's orbit can be found by setting $\dot{r} = 0$ in Eq. (2) and re-arranging the terms according to the cubic polynomial [19]

$$r^3 + \frac{\mu}{E} r^2 - \frac{H_0^2}{2E} r + \frac{J_0}{3E} = 0. \tag{4}$$

The roots of Eq. (4) are hereby referred to as $\alpha \geqslant \beta \geqslant \gamma$ and can be found using standard numerical procedures available in MATLAB* or Python's numpy [27]. The interested reader may refer to [28] for a more in-depth analysis of the characteristic polynomial given by Eq. (4), as well as of the 14 types of motion emerging from it. For planetary

*https://www.mathworks.com/

moons systems (i.e., $E < 0$, $H_0 > 8J_2$), the roots of the cubic polynomial are guaranteed to be positive, distinct, and real with [19]

$$\alpha + \beta + \gamma = -\frac{\mu}{E}, \tag{5a}$$

$$(\alpha\,\beta + \alpha\,\gamma + \beta\,\gamma) = -\frac{H_0^2}{2\,E}, \tag{5b}$$

$$\alpha\,\beta\,\gamma = -\frac{J_0}{3\,E}. \tag{5c}$$

It is worth noting that α corresponds to the farthest of the two intersections appearing in Fig. 2, whereas β corresponds to the intersection of Fig. 2 that is the closest to the surface of the host planet. The remaining root γ is empirically found to be located below the surface of the host planet (non-physical root), with $\gamma = 0$ whenever $J_2 = 0$. Such an observation plays a crucial role in enabling the homotopy continuation strategy proposed in this work. It is also the reason why we favor the analytical solution of the J_2-perturbed equatorial problem offered in Ref. 19 over the analytical developments available in Ref. 18. While the original derivation results in a simpler cubic polynomial rather than the quartic equation below (c.f., Eq. (8)), it leads to singularities in the equations of the Zonal Hill Problem whenever $J_2 = 0$. This is unacceptable for the purpose of this work, in which candidate spacecraft trajectories are intended to be continued from similar solutions obtained with $J_2 = 0$.

Accordingly, let us consider the analytical solution of Eq. (1b) and a change of independent variable as follows:

$$\frac{\mathrm{d}r}{\mathrm{d}t} = \frac{\mathrm{d}r}{\mathrm{d}\theta}\,\frac{\mathrm{d}\theta}{\mathrm{d}t} = r'\,\frac{H_0}{r^2}, \tag{6}$$

where primes $(-)'$ denote differentiation with respect to the true longitude of the secondary. Since $\dfrac{\mathrm{d}r}{\mathrm{d}t} = \dot{r}$, Eq. (2) can be squared on both sides and algebraically manipulated to get

$$\sqrt{3}\,H_0\,(r')^2 = (-6\,E)\,\left(-r^4 - \frac{\mu}{E}\,r^3 + \frac{H_0^2}{2\,E}\,r^2 - \frac{J_0}{3\,E}\,r\right), \tag{7}$$

with

$$\left(-r^4 - \frac{\mu}{E}\,r^3 + \frac{H_0^2}{2\,E}\,r^2 - \frac{J_0}{3\,E}\,r\right) = r\,(r-\alpha)\,(r-\beta)\,(r-\gamma) \tag{8}$$

in light of Eq. (4) and $\beta \leqslant r \leqslant \alpha$. Separation of variables further simplifies Eq. (7) into

$$\frac{\mathrm{d}r}{\sqrt{(r-\alpha)\,(r-\beta)\,(r-\gamma)\,r}} = \frac{\sqrt{-2\,E}}{H_0}\,\mathrm{d}\theta, \tag{9}$$

yielding [29]

$$\theta - \theta_0 = \omega_0\,(\tau - \tau_0), \tag{10}$$

where $\tau = F(\varphi, M)$ is the incomplete elliptic integral of the first kind, and

$$\varphi = \arcsin\left(\mathrm{sn}\tau\right), \tag{11a}$$

$$\mathrm{sn}^2\tau = \frac{(\alpha - r)\,\beta}{(\alpha - \beta)\,r}, \tag{11b}$$

$$M = \frac{(\alpha - \beta)\,\gamma}{(\alpha - \gamma)\,\beta}, \tag{11c}$$

$$g = \frac{2}{\sqrt{(\alpha - \gamma)\,\beta}}, \tag{11d}$$

$$\omega_0 = \frac{H_0}{\sqrt{-2\,E}}\,g. \tag{11e}$$

From Eq. (11b), it follows

$$r(\tau) = \frac{\alpha}{1 + m\,\mathrm{sn}^2(\tau)} = \frac{\alpha}{\Delta}, \tag{12a}$$

$$r'(\tau) = -n\,\mathrm{sn}(\tau)\,\mathrm{cn}(\tau)\,\mathrm{dn}(\tau)\,r^2, \tag{12b}$$

where $m = (\alpha - \beta)/\beta$ and $n = 2\,m/(\alpha\,\omega_0)$. Equation (12a) proves that the distance between the two primaries is a periodic function of τ with periodicity $2\,K$, where K is the complete elliptic integral of the first kind [29].

Note that θ_0 and τ_0 are often combined into a single variable [18] to rewrite Eq. (10) as

$$\theta = \theta_c + \omega_0\,\tau, \tag{13}$$

where

$$\theta_c = \theta_0 - \omega_0\,\tau_0. \tag{14}$$

The variable τ_0 is derived from the initial conditions (r_0, r_0') and set to

$$\tau_0 = \begin{cases} F(\varphi_0, M), & \text{if } \mathrm{cn}(\tau_0) \geqslant 0, \\ \\ 2\,K - F(\varphi_0, M), & \text{if } \mathrm{cn}(\tau_0) < 0, \end{cases} \tag{15}$$

depending on whether

$$\mathrm{cn}(\tau_0) = -\frac{1}{n\,\mathrm{sn}(\tau_0)\,\mathrm{dn}(\tau_0)}\left(\frac{r_0'}{r_0^2}\right) \tag{16}$$

is either positive or negative, respectively. Owing to the appearance of $\mathrm{sn}^2(\tau)$ in the denominator of Eq. (12a), $\mathrm{sn}(\tau_0)$

can be always assumed to be positive without loss of generality, whereas $\mathrm{dn}(\tau_0) = \sqrt{1 - M\,\mathrm{sn}^2(\tau_0)}$.

Figure 3 compares the position and velocity errors of Phobos' orbit with SPICE ephemerides. As can be seen, the analytical solution of the equatorial oblate problem maintains the position and velocity errors relatively bounded and below 100 km and 10 m/s, respectively. The error is dominated by the out-of-plane component ($J2_z$ in the plots), which is by design neglected in the analytical developments presented in this Section. For comparison, the relative error between the two-body propagation of Phobos and SPICE ephemerides is also shown in black to investigate the accuracy of the Martian moon's position and velocity knowledge over time. After 100 orbital periods (30 days circa), the two-body error is found to be one-to-two orders of magnitude larger than the J_2 equatorial one.

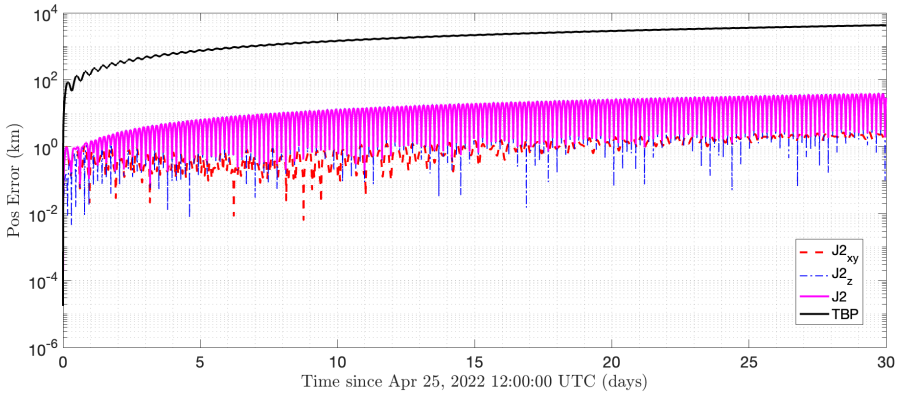

Fig. 3 Comparison between the TBP and J2 equatorial analytical propagation of Phobos' orbit. The position and velocity errors are obtained by comparison with SPICE ephemerides.

Similar error plots can be drawn for other planetary moon systems, as shown in Fig. 4. A pattern emerges according to which the zonal equatorial model significantly outperforms the Keplerian propagations by one or two orders of magnitude for planetary satellites whose distance from the host planet is approximately less than 10 host planet radii. Above this threshold, the J_2 perturbation becomes less relevant and dominated by other dynamical effects such as the third body attraction of other moons within the same planetary system (c.f., Fig. 4d). As shown in Fig. 5, the majority of the planetary moons of the solar system falls within this region with the notable exceptions of Ganymede, Callisto, and Titan.

We conclude this section by recalling that a Kepler-like equation for the time variable can be also deduced. Indeed, $\dot{\theta} = H_0/r^2$ implies

$$\frac{\mathrm{d}t}{\mathrm{d}\tau} = \frac{1}{\dot{\theta}}\frac{\mathrm{d}\theta}{\mathrm{d}\tau} = \frac{\omega_0}{H_0}\,r^2, \tag{17}$$

and

$$t - t_0 = \frac{\omega_0}{H_0}\int_{\tau_0}^{\tau}\left[\frac{\alpha}{1 + m\,\mathrm{sn}^2(\tau)}\right]^2 \mathrm{d}\,\tau. \tag{18}$$

An analytical solution of Eq. (18) is available in either [18] or [19] and involves a truncated series expansion in terms of

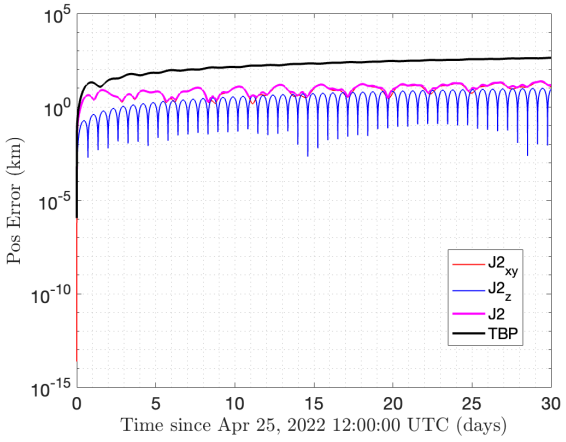

(a) Mars-Deimos

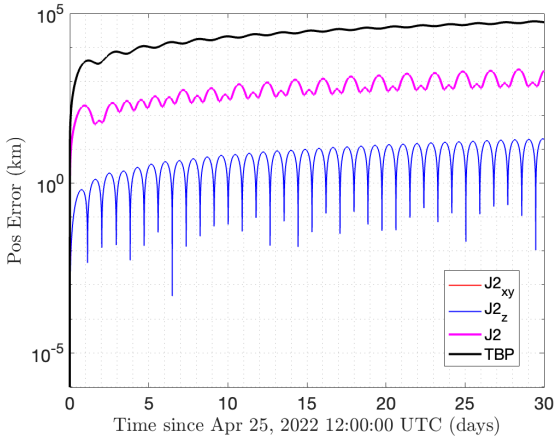

(b) Jupiter-Io

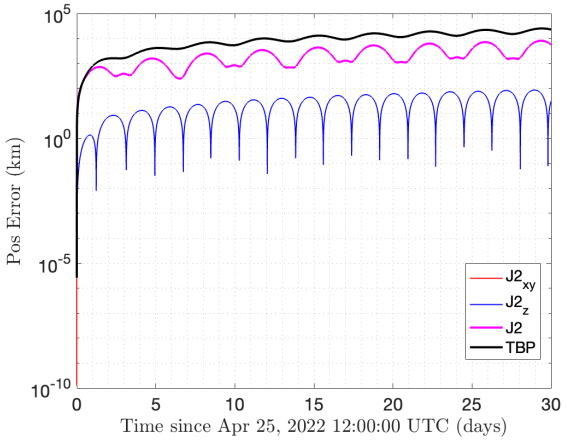

(c) Jupiter-Europa

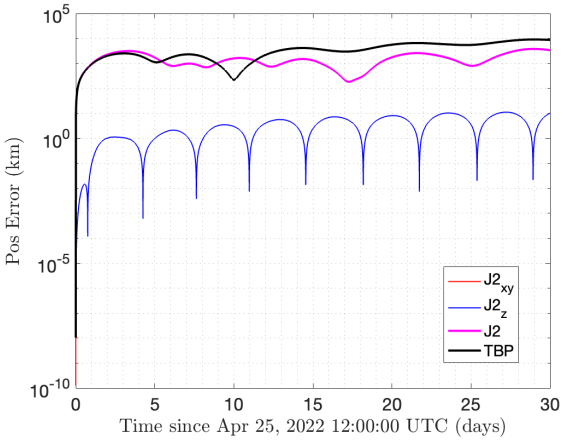

(d) Jupiter-Ganymede

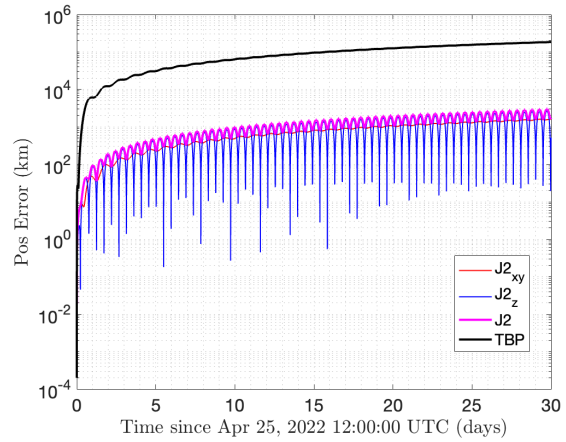

(e) Saturn-Mimas

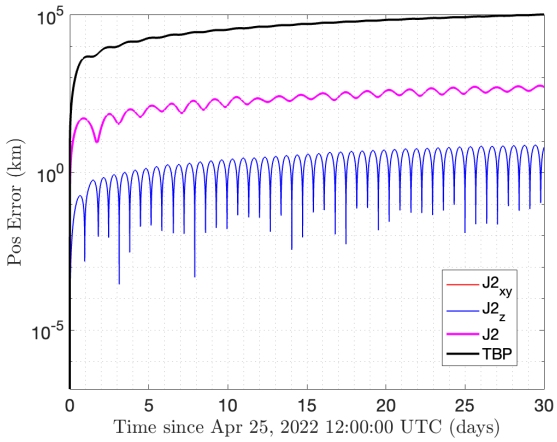

(f) Saturn-Enceladus

Fig. 4 Comparison between the TBP and the J2 equatorial analytical propagation of different planetary systems. All the plots display the absolute position error in logarithmic scale.

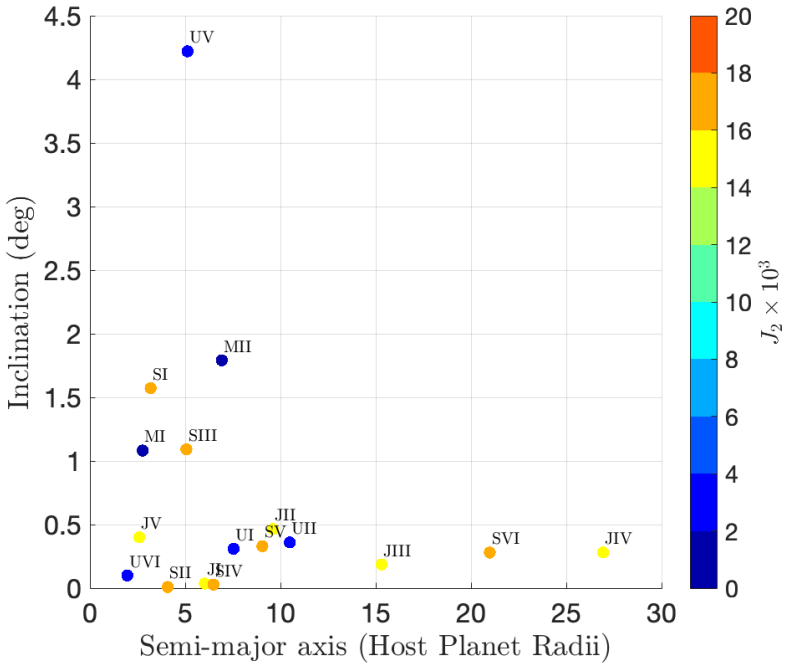

Fig. 5 Inclination versus semi-major axis plot for solar system moons. The color of each points refers to the J_2 oblateness of their corrisponding host planet.

trigonometric functions. For the purposes of this work, we find it sufficient to set $t_0 = 0$ and calculate the time elapsed since epoch via either the numerical evaluation of Eq. (18) or by appending Eq. (17) to the spacecraft equations of motion detailed in the following Section.

III. The Zonal Hill Problem

Let us now denote $\boldsymbol{\rho} = \begin{bmatrix} x, & y, & z \end{bmatrix}^T$ as the position vector of a massless particle with respect to the barycenter of the moon as shown in Fig. 6. The dynamical evolution of $\boldsymbol{\rho}$ can be described in a rotating reference frame centered on the secondary and such that $\hat{\boldsymbol{x}} = \boldsymbol{r}/\|\boldsymbol{r}\|$ is constantly aligned with the relative position vector of the two primaries, $\hat{\boldsymbol{z}}$ is parallel to the orbital angular momentum of the moon, and $\hat{\boldsymbol{y}} = \hat{\boldsymbol{z}} \times \hat{\boldsymbol{x}}$ completes the right-handed triad:

$$\ddot{\boldsymbol{\rho}} + \dot{\boldsymbol{\Omega}} \times \boldsymbol{\rho} + 2\,\boldsymbol{\Omega} \times \dot{\boldsymbol{\rho}} + \boldsymbol{\Omega} \times \boldsymbol{\Omega} \times \boldsymbol{\rho} = \nabla \mathcal{U}. \tag{19}$$

In Eq. (19), dots denote differentiation with respect to time t, $\Omega = \dot{\theta}\,\hat{\boldsymbol{z}} = \frac{H_0}{r^2}\,\hat{\boldsymbol{z}}$ is the angular velocity vector of the moon, and $\mathcal{U}$ is the gravitational potential given by

$$\mathcal{U} = \mathcal{U}_1 + \mathcal{U}_2 + \frac{\mu}{r^3}\,\boldsymbol{r}^T\boldsymbol{\rho} + \frac{J_0}{r^5}\,\boldsymbol{r}^T\boldsymbol{\rho}. \tag{20}$$

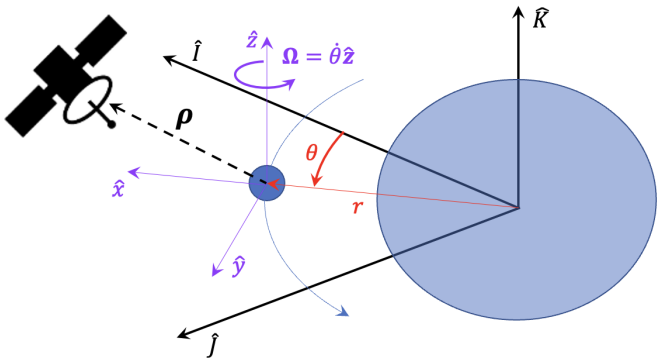

Fig. 6 Frames and dynamical quantities definitions for the Zonal Hill Problem.

The variables

$$\mathcal{U}_1 = \frac{\mu}{r_1} - \frac{1}{3}\frac{J_0}{r_1^3}\left(3\frac{z^2}{r_1^2} - 1\right), \tag{21}$$

$$\mathcal{U}_2 = \frac{\eta}{\rho}, \tag{22}$$

stand for the gravitational potentials of the primary and secondary body, respectively, with η as the gravitational parameter of the moon, and $\rho = \|\boldsymbol{\rho}\|$, $r_1 = \|\boldsymbol{r}_1\| = \|\boldsymbol{r} + \boldsymbol{\rho}\|$, $r = \|\boldsymbol{r}\|$. It is assumed that the gravitational potential of the moon has negligible effects on the motion of the planet, i.e., $\eta << \mu$. Under this assumption, Eq. (19) may be rewritten as

$$\boldsymbol{\rho}^{\star\star} - 2\frac{r^\star}{r}\boldsymbol{\rho}^\star - 2\,\omega_0\left[\frac{r^\star}{r}(\hat{\boldsymbol{z}}\times\boldsymbol{\rho}) - (\hat{\boldsymbol{z}}\times\boldsymbol{\rho}^\star)\right] + \omega_0^2(\hat{\boldsymbol{z}}\times\hat{\boldsymbol{z}}\times\boldsymbol{\rho}) = \frac{1}{f^2}\nabla\mathcal{U}, \tag{23}$$

where $(\cdot)^\star$ denotes differentiation with respect to τ, and

$$\dot{\boldsymbol{\rho}} = \boldsymbol{\rho}^\star f, \tag{24a}$$

$$\ddot{\boldsymbol{\rho}} = \boldsymbol{\rho}^{\star\star} f^2 + \boldsymbol{\rho}^\star f^\star f, \tag{24b}$$

$$\boldsymbol{\Omega} = f\,\omega_0\hat{\boldsymbol{z}}, \tag{24c}$$

$$\dot{\boldsymbol{\Omega}} = \omega_0 f^\star f\,\hat{\boldsymbol{z}}, \tag{24d}$$

$$f = \frac{\mathrm{d}\tau}{\mathrm{d}t} = \frac{\mathrm{d}\tau}{\mathrm{d}\theta}\dot{\theta} = \frac{H_0}{\omega_0}\frac{1}{r^2}, \tag{24e}$$

$$f^\star = -2\frac{r^\star}{r}f. \tag{24f}$$

Then, introducing pulsating coordinates such that $\boldsymbol{\rho} = \bar{\eta}\,r\,\tilde{\boldsymbol{\rho}}$, where $\bar{\eta} = \left(\frac{\eta}{\mu}\right)^{(1/3)}$ is the cubic root of the mass ratio between the two primaries, yields

$$\tilde{\boldsymbol{\rho}}^{\star\star} - h\,\tilde{\boldsymbol{\rho}} + 2\,\omega_0(\hat{\boldsymbol{z}}\times\tilde{\boldsymbol{\rho}}^\star) + \omega_0^2(\hat{\boldsymbol{z}}\times\hat{\boldsymbol{z}}\times\tilde{\boldsymbol{\rho}}) = \left(\frac{1}{\bar{\eta}^2\,r^2\,f^2}\right)\tilde{\nabla}\mathcal{U}, \tag{25}$$

with

$$h(\tau) := \frac{2\,m\,\left(\mathrm{cn}^2(\tau)\,\mathrm{dn}^2(\tau) - \mathrm{sn}^2(\tau)\,\mathrm{dn}^2(\tau) - M\,\mathrm{sn}^2(\tau)\,\mathrm{cn}^2(\tau)\right)}{\Delta}, \tag{26}$$

and $\tilde{\nabla}$ as the gradient with respect to the nondimensional vector $\tilde{\boldsymbol{\rho}}$.

If $\rho << r$, Eq. (21) can be expanded about r up to the second order in ρ:

$$\begin{aligned}\mathcal{U}_1 \simeq \frac{\mu}{r} + \frac{J_0}{3\,r^3} - \frac{J_0}{r^5}\,\boldsymbol{\rho}^T\,\hat{\boldsymbol{z}}\,\hat{\boldsymbol{z}}^T\,\boldsymbol{\rho}\ldots \\ - \frac{\mu}{r^3}\,\boldsymbol{r}^T\boldsymbol{\rho} - \frac{J_0}{r^5}\,\boldsymbol{r}^T\boldsymbol{\rho}\ldots \\ + \frac{\mu}{2\,r^3}\,\boldsymbol{\rho}^T\,\left(-I + 3\,\hat{\boldsymbol{x}}\,\hat{\boldsymbol{x}}^T\right)\,\boldsymbol{\rho}\ldots \\ + \frac{J_0}{2\,r^5}\,\boldsymbol{\rho}^T\,\left(-I + 5\,\hat{\boldsymbol{x}}\,\hat{\boldsymbol{x}}^T\right)\,\boldsymbol{\rho},\end{aligned} \tag{27}$$

where I is the 3-by-3 identity matrix. Then, Eq. (20) can be simplified in

$$\mathcal{U} \simeq \mathcal{U}_2 + \frac{\mu}{2\,r^3}\,\boldsymbol{\rho}^T\,J\,\boldsymbol{\rho} + \frac{J_0}{2\,r^5}\,\boldsymbol{\rho}^T\,K\,\boldsymbol{\rho} \tag{28}$$

where

$$J = \begin{bmatrix} 2 & 0 & 0 \\ 0 & -1 & 0 \\ 0 & 0 & -1 \end{bmatrix}, \tag{29a}$$

$$K = \begin{bmatrix} 4 & 0 & 0 \\ 0 & -1 & 0 \\ 0 & 0 & -3 \end{bmatrix}, \tag{29b}$$

and without taking into account terms of Eq. (27) that do not depend explicitly on the spacecraft's position vector. Finally, the expression of the gravitational potential becomes:

$$\mathcal{U} \simeq \bar{\eta}^2\,\frac{\mu}{r}\,\tilde{\mathcal{U}}, \tag{30}$$

where

$$\tilde{\mathcal{U}} = \frac{1}{\tilde{\rho}} + \frac{1}{2}\,\tilde{\boldsymbol{\rho}}^T\,\left(J + \frac{3}{2}\,\bar{J}_2\,\Delta^2\,K\right)\,\tilde{\boldsymbol{\rho}}, \tag{31}$$

and

$$\bar{J}_2 = J_2 \left(\frac{R_e}{\alpha}\right)^2. \tag{32}$$

Substituting Eq. (30) into (25) yields

$$\tilde{\boldsymbol{\rho}}^{\star\star} + 2\,\omega_0\,(\hat{\boldsymbol{z}} \times \tilde{\boldsymbol{\rho}}^{\star}) = \omega_0^2\,\tilde{\nabla}\tilde{\mathcal{W}}, \tag{33}$$

where

$$\tilde{\mathcal{W}} = \left[\frac{\bar{\mu}}{\Delta}\,\tilde{\mathcal{U}} + \frac{1}{2}\,\tilde{\boldsymbol{\rho}}^T\,(H - Z\,Z)\,\tilde{\boldsymbol{\rho}}\right], \tag{34a}$$

$$\bar{\mu} = \frac{\mu\,\alpha}{H_0^2}, \tag{34b}$$

$$H = \bar{h}\,\frac{\Gamma}{\Delta}\,I, \tag{34c}$$

$$\bar{h} = \frac{2\,m}{\omega_0^2}, \tag{34d}$$

$$\Gamma(\tau) = \left(\mathrm{cn}^2(\tau)\,\mathrm{dn}^2(\tau) - \mathrm{sn}^2(\tau)\,\mathrm{dn}^2(\tau) - M\,\mathrm{sn}^2(\tau)\,\mathrm{cn}^2(\tau)\right), \tag{34e}$$

$$Z = \begin{bmatrix} 0 & -1 & 0 \\ 1 & 0 & 0 \\ 0 & 0 & 0 \end{bmatrix}. \tag{34f}$$

It follows that

$$\begin{cases} \tilde{x}^{\star\star} - 2\,\omega_0\,\tilde{y}^{\star} &= \omega_0^2\,\tilde{\mathcal{W}}_{\tilde{x}}, \\ \tilde{y}^{\star\star} + 2\,\omega_0\,\tilde{x}^{\star} &= \omega_0^2\,\tilde{\mathcal{W}}_{\tilde{y}}, \\ \tilde{z}^{\star\star} &= \omega_0^2\,\tilde{\mathcal{W}}_{\tilde{z}}, \end{cases} \tag{35}$$

where

$$\tilde{\mathcal{W}}_{\tilde{x}} = \left[\frac{\bar{\mu}}{\Delta}\left(-\frac{1}{\tilde{\rho}^3} + 2 + 6\,\bar{J}_2\,\Delta^2\right) + 1 + \bar{h}\,\frac{\Gamma}{\Delta}\right]\tilde{x}, \tag{36a}$$

$$\tilde{\mathcal{W}}_{\tilde{y}} = \left[\frac{\bar{\mu}}{\Delta}\left(-\frac{1}{\tilde{\rho}^3} - 1 - \frac{3}{2}\,\bar{J}_2\,\Delta^2\right) + 1 + \bar{h}\,\frac{\Gamma}{\Delta}\right]\tilde{y}, \tag{36b}$$

$$\tilde{\mathcal{W}}_{\tilde{z}} = \left[\frac{\bar{\mu}}{\Delta}\left(-\frac{1}{\tilde{\rho}^3} - 1 - \frac{9}{2}\,\bar{J}_2\,\Delta^2\right) + \bar{h}\,\frac{\Gamma}{\Delta}\right]\tilde{z}. \tag{36c}$$

Eq. (35) can be further simplified by introducing $\nu = \tau/\omega_0$ as the final independent variable of the system:

$$\begin{cases} \tilde{x}'' - 2\,\tilde{y}' &= \tilde{\mathcal{W}}_{\tilde{x}}, \\ \tilde{y}'' + 2\,\tilde{x}' &= \tilde{\mathcal{W}}_{\tilde{y}}, \\ \tilde{z}'' &= \tilde{\mathcal{W}}_{\tilde{z}}, \end{cases} \tag{37}$$

where $(\cdot)'$ denote differentiation with respect to ν. It is worth noting that $\theta = \theta_c + \omega_0\,\tau = \theta_c + \nu$ implies $\dfrac{\mathrm{d}(\,)}{\mathrm{d}\nu} = \dfrac{\mathrm{d}(\,)}{\mathrm{d}\theta}$, thus explaining the choice of $(\cdot)'$ as the differentiation symbol. However, we highlight that θ and ν vary across different domains, with the former being defined over $[0, 2\,\pi]$ and the latter spanning across $[0, 2\,K\,\omega_0]$. A quick derivation provided in the appendix can also demonstrate how the system (37) reduces to the equations of the elliptical Hill problem [14] when $J_2 = 0$.

IV. Solutions of Interest

The equations of the ZHP can be rewritten as a system of first-order ordinary differential equations via

$$\boldsymbol{X}' = \boldsymbol{h}(\nu, \boldsymbol{X}, \boldsymbol{p}) = \begin{cases} \tilde{u}, \\ \tilde{v}, \\ \tilde{w}, \\ \tilde{\mathcal{W}}_{\tilde{x}} + 2\,v, \\ \tilde{\mathcal{W}}_{\tilde{y}} - 2\,u, \\ \tilde{\mathcal{W}}_{\tilde{z}}, \end{cases} \tag{38}$$

where $\boldsymbol{X} = \begin{bmatrix} \tilde{x}, & \tilde{y}, & \tilde{z}, & \tilde{u}, & \tilde{v}, & \tilde{w} \end{bmatrix}$, and $\boldsymbol{p} = \begin{bmatrix} \bar{\mu}, & \bar{J}_2, & m, & \omega_0 \end{bmatrix}$. Eq. (38) depends explicitly on the independent variable ν via the Δ terms appearing in Eq. (36) and is T-periodic with $T = 2\,K\,\omega_0$:

$$\boldsymbol{h}(\nu + T, \boldsymbol{X}, \boldsymbol{p}) = \boldsymbol{h}(\nu, \boldsymbol{X}, \boldsymbol{p}).$$

As a non-autonomous time-periodic system, the ZHP admits isolated resonant periodic orbits along with families of two-dimensional quasi-periodic invariant tori that replace the continuum of periodic orbits found in its autonomous counterpart, i.e., the Circular Hill Problem (CHP) [30]. Starting from the equilibrium points and periodic orbits available in the literature, an homotopy continuation approach can be implemented to locate periodic and quasi-periodic solutions of Eq. (38) [16, 31, 32]. Examples of both of these *dynamical substitutes* can be found in the following subsections.

A. Dynamical Substitutes of Equilibrium Points

The CHP is known to have two equilibrium points along the host-planet and anti-host-planet directions[8]. These equilibrium points are typically referred to as L_1 and L_2 and have CHP normalized coordinates given by $\begin{bmatrix} -\sqrt[3]{1/3} & 0 & 0 & 0 & 0 & 0 \end{bmatrix}$ and $\begin{bmatrix} \sqrt[3]{1/3} & 0 & 0 & 0 & 0 & 0 \end{bmatrix}$, respectively. The original coordinates remain valid in the elliptical Hill problem while using pulsating normalized coordinates to search for candidate periodic orbits that would substitute the original equilibrium points near the surface of the planetary moon. Indeed, the same periodic orbits can be also found in the ZHP while setting the J_2 of the host planet to zero (see Appendix for proof).

By gradually increasing the value of J_2 till a desired upper bound (e.g., the second zonal harmonics coefficient of Saturn, $J_2 = 0.016298$) it is possible to grow the original solutions under the influence of the oblateness of the host planet. Figure 7 showcases examples of resonant periodic orbits ($T = 2\,K\,\omega_0$ as for the period of the planetary moon around the host planet) as seen with respect to the surface of Phobos, Io, and Enceladus, respectively.

In all cases, the differential correction of the trajectory is carried out using a collocation method with 101 nodes and 7-th order Lagrange polynomials [20, 32]. The algorithm seeks for solutions of the two-point boundary value problem given by Eq. (38) and the boundary conditions

$$\boldsymbol{c}(\boldsymbol{X}_0, \boldsymbol{X}_T) := \boldsymbol{X}_T - \boldsymbol{X}_0 = \boldsymbol{0}, \tag{39}$$

where $\boldsymbol{X}_0$ and $\boldsymbol{X}_T$ are the initial and final conditions of the spacecraft after time $T = 2\,K\,\omega_0$, respectively. Notice that phase conditions and parametrizing equations do not need to be included into the constraint vector $\boldsymbol{c}$, owing to the time-dependent nature of the problem and the fact that existing periodic orbits would be isolated at best[9, 33]. In principle, pseudo-arclength continuation should be appended to Eq. (39) with J_2 as a *free* varying variable in the predictor-corrector algorithm arising from the numerical solution of the two-point boundary value problem [34]. However, this step was deemed unnecessary after noticing that quadratic convergence could be achieved in 3 to 5 iterations for all $J_2 \in [0, 0.016298]$ and different planetary moon systems.

The resulting trajectories follow a closed egg-shaped path which is the farthest from the planetary moon when $\nu = 0$ (corresponding to the moon being at the apoapsis of its orbit around the host planet). Both the L_1 and L_2 dynamical substitutes evolve in a counter-clockwise direction as seen from the top of the planet's equatorial plane. All orbits are found to be highly unstable with a maximum monodromy matrix eigenvalue of approximately 7×10^6. Consequently, stable and unstable manifolds emanate from each of the L1 (first row) and L2 (second row) dynamical substitutes as shown in Figure 8. We choose the Saturn-Enceladus system as an example, although similar plots can be drawn for any arbitrary planetary moon system. The two-dimensional manifolds shadow the stable and unstable manifolds of the CHP until they intersect the surface of the planetary satellite at a longitude and impact angle that depends on the physical parameters of the problem. States remain located in the equatorial plane of the host planet regardless of the different ν

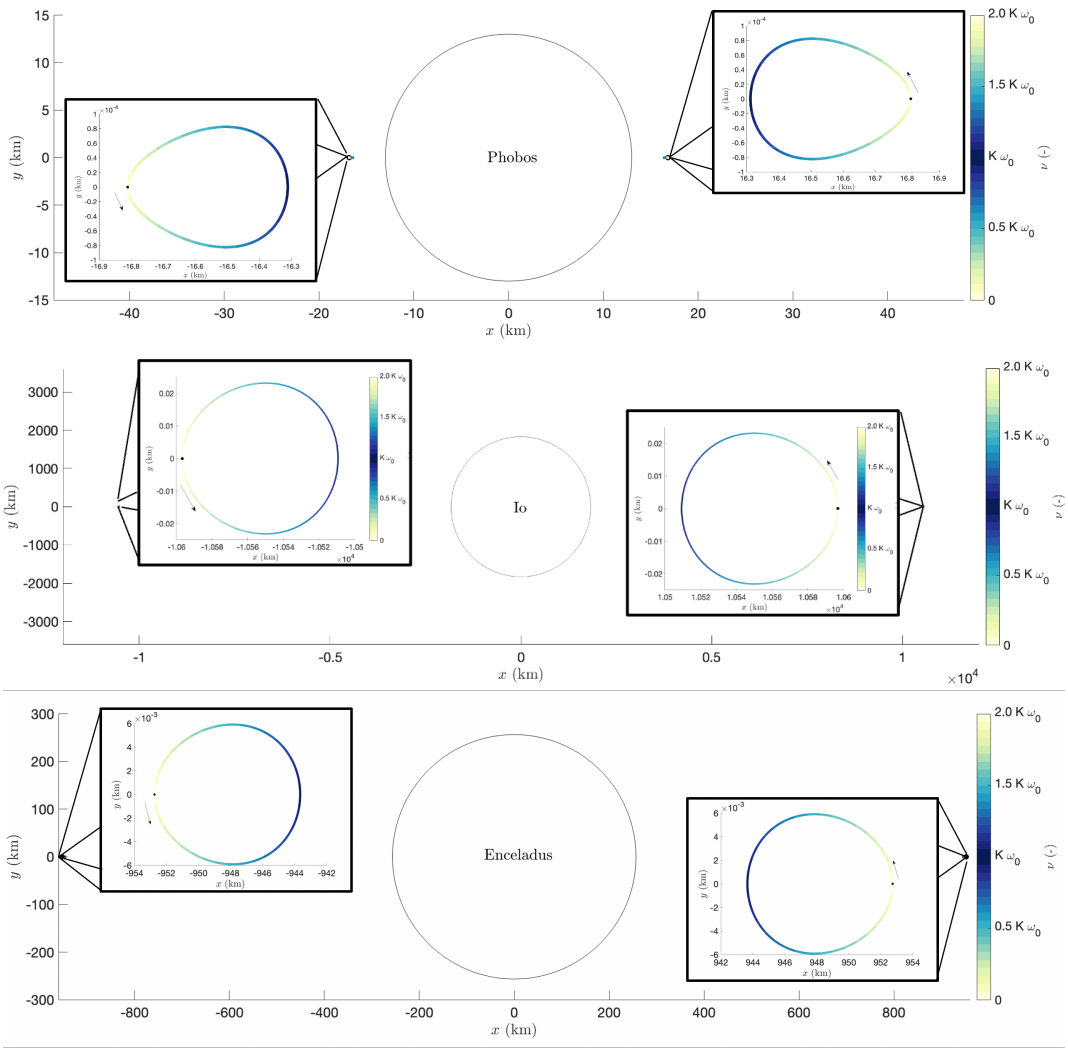

Fig. 7 From top to bottom: Equilibrium points dynamical substitutes in the ZHP for Phobos (Mars' $J_2 = 1960.45 \times 10^{-6}$), Io (Jupiter's $J_2 = 0.014736$), and Enceladus (Saturn's $J_2 = 0.016298$).

values encountered throughout the numerical propagation of the 70 spacecraft trajectories utilized to approximate the two-dimensional invariant surfaces (see color code of Fig. 8).

B. Dynamical Substitutes of Periodic Orbits

Similarly to equilibrium points, periodic orbits found under the assumptions of the CHP can be also continued in the ZHP by noticing that the resulting invariant sets would be of dimension one more [31, 32]. It follows that entire families of two-dimensional quasi-periodic invariant tori can be generated starting from databases of CHP periodic orbits available in the literature [12, 30].

Recall that computing a two-dimensional quasi-periodic invariant torus is equivalent to finding a numerical approximation for a diffeomorphism $\boldsymbol{u}(\boldsymbol{\theta}) : [0, 2\pi] \times [0, 2\pi] \rightarrow \mathcal{T} \in \mathbb{R}^6$ such that motion on the surface of $\mathcal{T}$ can be

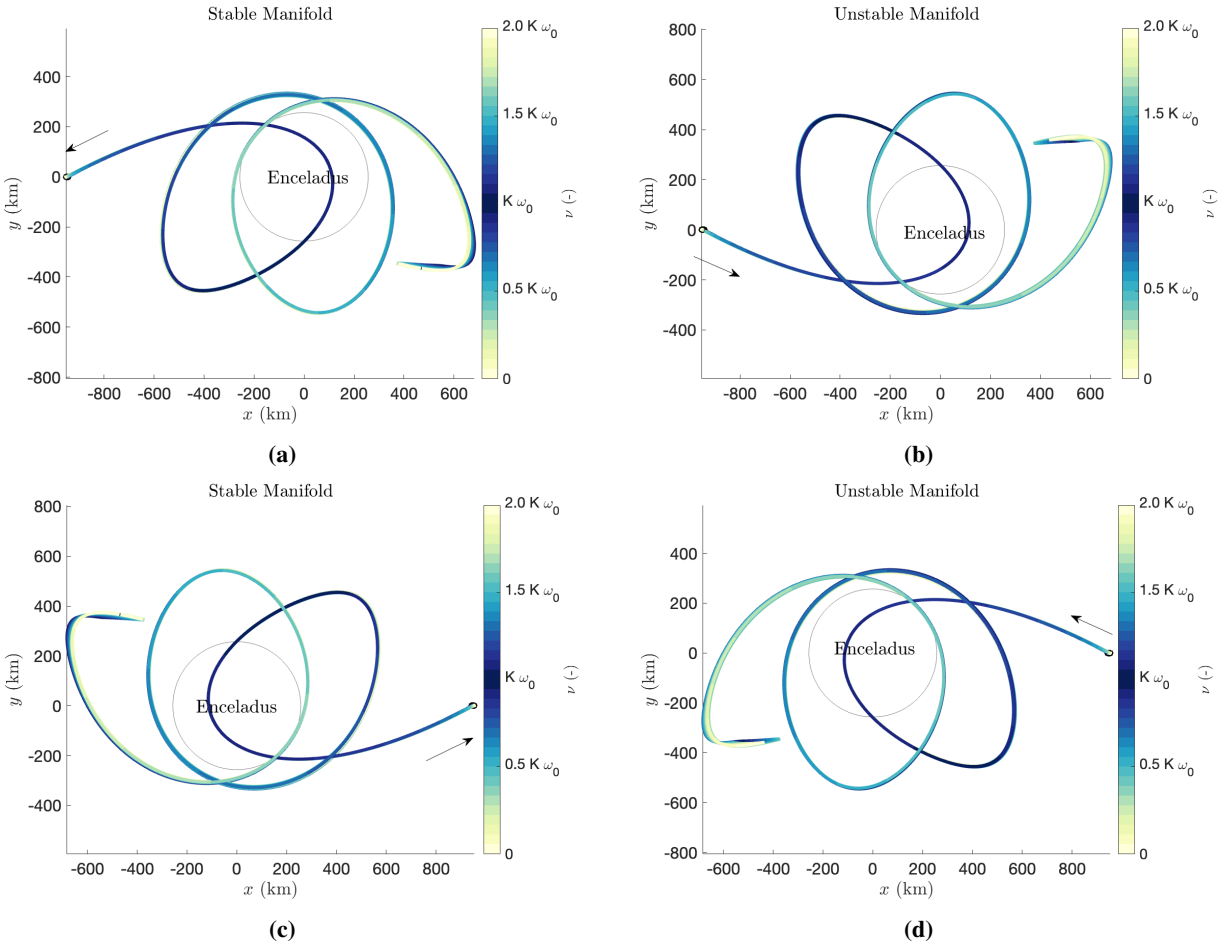

Fig. 8 Stable and Unstable manifolds emanating from the L1 (top) and L2 (bottom) dynamical substitutes.

characterized by two incommensurate frequencies: $\boldsymbol{\theta}' = \boldsymbol{\omega} = \begin{bmatrix} \omega_1 & \omega_2 \end{bmatrix}^T \in \mathbb{R}^2$ [35]. The first of these two frequencies is usually referred to as the longitudinal or toroidal frequency of the manifold, whereas the latter is often referred to as the latitudinal or poloidal one. As long as $\omega_1/\omega_2 \notin \mathbb{Z}$, quasi-periodic trajectories on the surface of $\mathcal{T}$ will densely cover the manifold as time grows to infinity. It is also expected that the angular variable θ_2 would be rotated by an angular quantity $\rho = \omega_2 P$ during the time span of a full revolution in the toroidal direction θ_1 (i.e., $P = 2\pi/\omega_1$). The quantity ρ is known in the dynamical systems theory literature as the rotation number of a torus [35]. Given $\boldsymbol{u}(\cdot)$, P, and ρ, motion on the surface of the manifold can be fully characterized at all times, thus enabling insight into the chaotic dynamics of the ZHP.

In order to calculate two-dimensional invariant tori, the GMOS algorithm available in the literature [21–24] is hereby modified to account for time-periodic effects as shown in [16, 32, 36, 37]. The main idea is that each point of a CHP periodic orbit $\boldsymbol{X}(t)$, $t \in [0, P]$ should transform into a one-dimensional curve $C_t := \{\boldsymbol{X} | \boldsymbol{X} = \boldsymbol{u}(t, \theta_2), \forall \theta_2 \in [0, 2\pi]\}$ as shown in Figure 9. Associating t with the longitudinal direction of a torus ($\theta_1 = 2\pi t/P$) enables re-defining C_t as

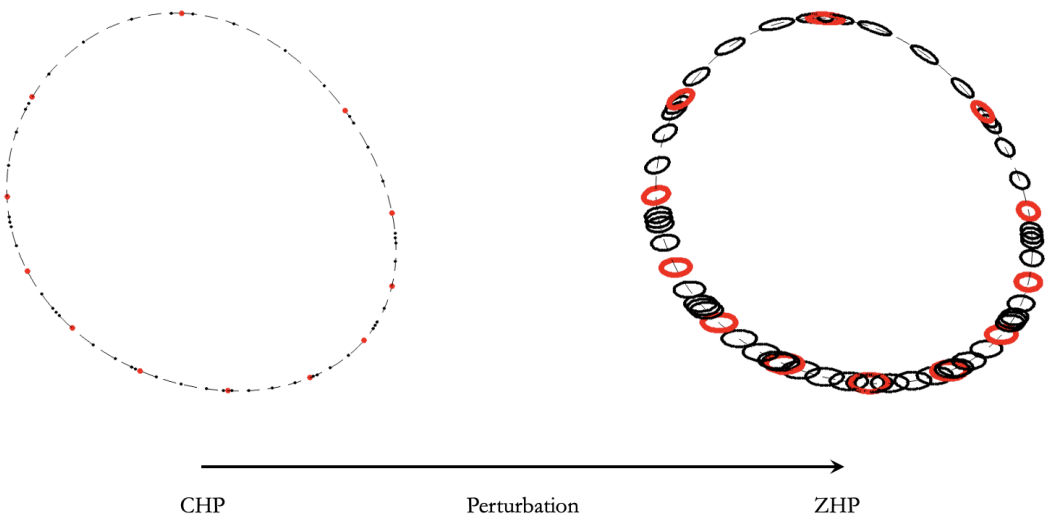

Fig. 9 Transition from CHP periodic orbits to ZHP quasi-periodic trajectories.

$C_{\theta_1} := \{\boldsymbol{X} | \boldsymbol{X} = \boldsymbol{u}(\theta_1, \theta_2), \forall \theta_2 \in [0, 2\pi]\}$ and demonstrates how C_{θ_1} must be invariant under the stroboscopic mapping $\varphi_P : \mathbb{R}^6 \to \mathbb{R}^6$ defined by the solution flow of (38) evaluated over time P. Indeed, for motion on a two-dimensional torus,

$$\begin{aligned} \varphi_P(\boldsymbol{u}(\theta_1, \theta_2)) &= \boldsymbol{u}(\theta_1 + \omega_1 P, \theta_2 + \omega_2 P), \\ &= \boldsymbol{u}(\theta_1 + 2\pi, \theta_2 + \rho), \\ &= \boldsymbol{u}(\theta_1, \theta_2 + \rho) \in C_{\theta_1}. \end{aligned} \tag{40}$$

Let us now denote

$$\boldsymbol{Z}_0 = \left[\boldsymbol{u}\,(\theta_1, 0)^T, \quad \boldsymbol{u}\left(\theta_1, \frac{2\pi}{N}\right)^T, \quad \ldots, \quad \boldsymbol{u}\left(\theta_1, \frac{2\pi\,(N-1)}{N}\right)^T \right]^T \tag{41}$$

as the collection of N equally spaced points along the candidate invariant curve C_{θ_1}, with $\theta_2 = 2\pi\, n/N, n = 0, \ldots, N-1$. For time-periodic systems like Eq. (38), the poloidal angular variable of the quasi-periodic torus is often associated with the independent variable of the problem. In the case of the ZHP,

$$\theta_2 = 2\pi\, \nu/(2\, K\, \omega_0) \tag{42}$$

implies that each of the candidate quasi-periodic trajectories in Eq. (41) corresponds to a specific phasing between the

planetary moon and its host planet. Furthermore,

$$\theta_2' = \omega_2 = 2\,\pi/(2\,K\,\omega_0), \tag{43}$$

and

$$\rho = 2\,\pi\,P/(2\,K\,\omega_0), \tag{44}$$

where P is the period of the original CHP periodic orbit.

Having fixed P and ρ, it is now possible to integrate the equations of motion (38) for each of the N candidate quasi-periodic trajectories and undo the poloidal rotation caused by the latitudinal frequency of the torus by means of the Discrete Fourier Transform (DFT)[23]. Given

$$\boldsymbol{Z}_P = \left[\boldsymbol{u}\,(\theta_1,\rho)^T,\quad \boldsymbol{u}\left(\theta_1,\frac{2\,\pi}{N}+\rho\right)^T,\quad \ldots,\quad \boldsymbol{u}\left(\theta_1,\frac{2\,\pi\,(N-1)}{N}+\rho\right)^T\right]^T, \tag{45}$$

one can calculate the Fourier coefficients of C_{θ_1} via

$$\hat{\boldsymbol{u}}_P[k] = \sum_{n=0}^{N-1} \boldsymbol{u}\left(\theta_1,\frac{2\pi\,n}{N}+\rho\right)\,e^{-2\pi j(n\,k/N)}, \tag{46}$$

and obtain a numerical approximation for any arbitrary point on C_{θ_1}, including

$$\begin{aligned}\boldsymbol{u}(\theta_1,\theta_2-\rho) &= R_{-\rho}[\boldsymbol{u}(\theta_1,\theta_2)],\\ &= \frac{1}{N}\sum_{k=0}^{N-1}\hat{\boldsymbol{u}}_P[k]\,e^{j\,k\,(\theta_2-\rho)},\\ &= \frac{1}{N}\sum_{k=0}^{N-1}\hat{\boldsymbol{u}}'_P[k]\,e^{j\,k\,\theta_2}.\end{aligned} \tag{47}$$

Equation (47) demonstrates the effects of a rotation operator $R_{-\rho}$, which acts on the Fourier coefficients of C_{θ_1} in order to rotate the ensemble of the N equally spaced points $\boldsymbol{Z}_P$ by an angular quantity $-\rho$. Rewritten in matrix form, Eq. (47) becomes

$$[R_{-\rho}] = [D^{-1}][Q_{-\rho}][D], \tag{48}$$

where $[D]$ and $[D^{-1}]$ are the DFT and inverse DFT matrices, respectively, and $[Q_{-\rho}]$ is a diagonal matrix that rotates the Fourier coefficients $\hat{\boldsymbol{u}}_P[k]$ of C_{θ_1} by $e^{-j\,k\,\rho}$ [24, 37].

Combined with Eq. (41) and (45), Eq. (48) yields a set of $6\,N$ constraints that must be satisfied by any collection of

N equally spaced points $\boldsymbol{Z}_0$ along any arbitrary invariant curve C_{θ_1} of φ_P:

$$\boldsymbol{G}(\boldsymbol{Z}_0, \boldsymbol{Z}_P) := [R_{-\rho}]\boldsymbol{Z}_P - \boldsymbol{Z}_0 = \boldsymbol{0}. \tag{49}$$

The degeneracy along the longitudinal direction of the torus can be removed with the addition of a phase condition

$$p(\boldsymbol{Z}_0) := \left\langle \boldsymbol{Z}_0 - \tilde{\boldsymbol{Z}}_0, \frac{\partial \tilde{\boldsymbol{Z}}_0}{\partial \theta_2} \right\rangle = 0 \tag{50}$$

in which $\tilde{\boldsymbol{Z}}_0$ denotes a previously known solution obtained from either the last iteration or the initial guess of the numerical continuation procedure. The final nonlinear set of equations given by Eq. (49) and (50) defines a well-posed, $(6\,N + 1)$-dimensional, two-point, boundary value problem that can be solved iteratively by means of Newton's method with

$$\boldsymbol{Z}_0 \simeq \tilde{\boldsymbol{Z}}_0 = \left[\boldsymbol{X}^T(0), \quad \boldsymbol{X}^T(0), \quad \ldots, \quad \boldsymbol{X}^T(0) \right]^T \in \mathbb{R}^{6\,N} \tag{51}$$

as an inaccurate initial guess.

In Eq. (51), $\boldsymbol{X}(0)$ represents the initial conditions of the original CHP periodic orbits, which are simply repeated over $\theta_2 = 2\,\pi\,n/N$, $n = 0, \ldots, N-1$ to generate a rough approximation of the first invariant curve. Regardless of this coarse approximation, the collocation version of the GMOS algorithm successfully converges onto a quasi-periodic invariant torus with $J_2 = 0$ after 4 to 7 iterations. The value of the host planet's oblateness is later increased until the original CHP periodic orbit is fully transitioned into the ZHP of the planetary system under consideration (10 steps till the actual J_2 value of the planet is reached). The proposed approach is an example of a zeroth-order homotopy continuation [34] since the J_2 of the planet is actually kept constant throughout the corrector part of the algorithm. This formulation spares users from calculating the partial derivatives of Eq. (49) with respect to J_2 and does not seem to affect the robustness nor the quadratic convergence of Newton's method. For the same reasons, the rotation number ρ is also not included in the vector of unknowns, but only updated in the predictor part of the algorithm to the theoretical value of Eq. (44).

Figure 10 illustrates several examples of two-dimensional quasi-periodic orbits obtained in the ZHP of the Mars-Phobos, Jupiter-Io, and Saturn-Enceladus systems. All of the invariant manifolds have been generated with 101 collocation nodes and 7-th order Lagrange polynomials, similarly to the dynamical substitutes of the L_1 and L_2 equilibrium points. The candidate trajectories for the zeroth-order homotopy continuation were arbitrarily picked from a pre-computed database of quasi-satellite, L_2 northern halo, and L_1 Lyapunov planar orbits with $P = 5.0$, 2.5 and 3.5 in CHP normalized units, respectively. Zoom-ins of the final solutions (i.e., the ones with $J_2 = 1960.45 \times 10^{-6}$, $J_2 = 0.014736$, and $J_2 = 0.016298$) are included in the plots to demonstrate the transition of the original periodic orbit into a collection of one-dimensional invariant curves for the stroboscopic mapping φ_P. A color code is also used

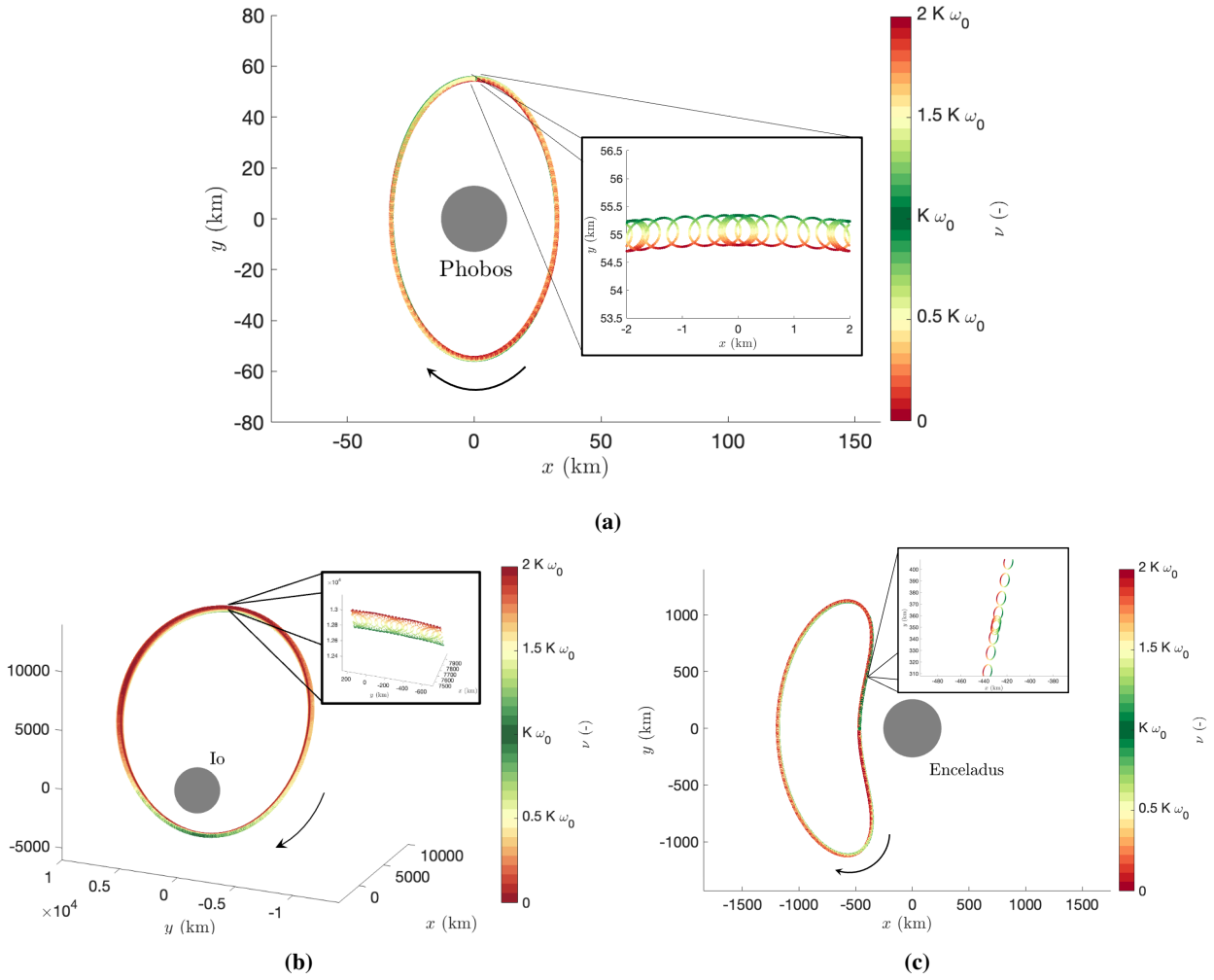

Fig. 10 Examples of Quasi-periodic invariant tori in the ZHP. a) Dynamical substitute of a quasi-satellite orbit around Mars with $P = 5.0$ in CHP normalized units; b) Quasi-halo torus near the Jupiter-Io L_2 orbit with $P = 2.5$; a) Dynamical substitute of a L_1 Lyapunov planar orbit with $P = 3.5$ in CHP normalized units.

to showcase the relationship between the poloidal angle of the torus and the phasing of the moon's orbit around the host planet. For both the invariant tori around Io and Enceladus, it is found that quasi-periodic trajectories would be the closer to the planetary moon the closer the latter is with respect to the surface of its host planet (ν values around $K\,\omega_0$, corresponding to the moon's periapsis). Along the leading and trailing edges of Phobos, instead, the spacecraft would be the closest to the surface of the Martian moon when $\mathrm{mod}(\nu, 2\,K\,\omega_0) \simeq 0$. A stability analysis enabled by the GMOS algorithm also confirms that retrograde quasi-periodic orbits around Phobos would remain stable even in the presence of Mars' J_2 perturbations. Similarly, stable and unstable manifolds are confirmed to emanate from the dynamical substitutes of the northern L_2 halo and L_1 Lyapunov planar orbits found in the vicinity of Io and Enceladus, respectively. The computed quasi-periodic trajectories are portrayed in Fig. 11 and enable high-fidelity transfer analyses near the surface of these planetary moons.

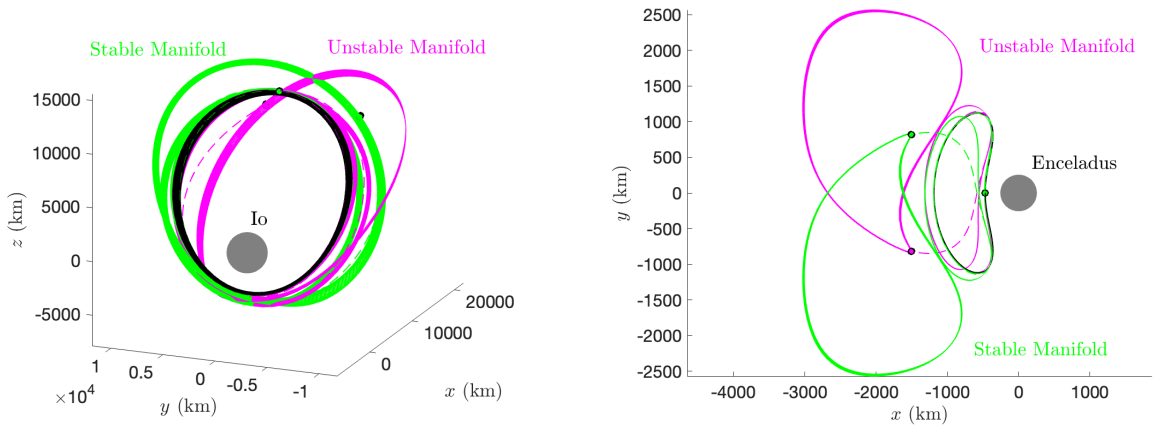

(a) **(b)**

Fig. 11 Stable and unstable manifolds emanating from hyperbolic quasi-periodic tori near Io (a) and Enceladus (b).

V. Conclusions

This paper introduced the equations of the ZHP to enable new and higher-fidelity simulations of the dynamics of spacecraft near planetary moons. The equations of motion were found to be non-autonomous and time-periodic, as it follows from the analytical solution of the zonal equatorial problem between the planetary moon and its host planet. A zeroth order homotopy continuation was therefore proposed to include the oblateness of the host planet into the dynamical evolution of a spacecraft, as well as transition equilibrium points and periodic orbits into their periodic and quasi-periodic dynamical substitutes. Our algorithm is based on the collocation formulation of the GMOS algorithm, enabling fast and robust calculation of two-dimensional invariant tori that populate the phase space of the ZHP. Examples of novel and higher-fidelity trajectories in the vicinity of Phobos, Io and Europa were presented, along with stable and unstable manifolds emanating from newly found hyperbolic solutions.

A. Appendix: Reduction to Elliptical Hill Problem when $J_2 = 0$

When $J_2 = 0$, the third root emerging from Eq. (4) is also equal to zero (i.e., $\gamma = 0$). Therefore, $M = 0$, $g = 2/\sqrt{\alpha\beta} = 2/\sqrt{a^2(1-e^2)}$, and $\omega_0 = 2$. From $r = \dfrac{a(1-e^2)}{1+e\cos(f)} = \dfrac{\alpha}{\Delta}$, it also follows that

$$\mathrm{sn}^2(\nu/\omega_0) = \mathrm{sn}^2(\tau) = \cos^2(f/2), \tag{52}$$

where f is the true anomaly of Phobos, along with $\mathrm{cn}(\tau)^2 = 1 - \mathrm{sn}^2(\tau) = \sin^2(f/2)$ and $\mathrm{dn}(\tau) = 1$.

The term $\dfrac{\bar{\mu}}{\Delta}$ can be now manipulated into

$$\frac{\bar{\mu}}{\Delta} = \frac{\mu}{H_0^2}\, r = \frac{1}{1 + e\, \cos f}, \tag{53}$$

whereas

$$\begin{aligned} \bar{h}\, \frac{\Gamma}{\Delta} &= \frac{m}{2}\, \frac{(\mathrm{cn}^2(\tau) - \mathrm{sn}^2(\tau))}{1 + m\, \mathrm{sn}^2(\tau)}, \\ &= \frac{m}{2}\, \frac{(\sin^2(f/2) - \cos^2(f/2))}{1 + m\, \sin^2(\tau)}, \\ &= -\frac{e\, \cos(f)}{1 + e\, \cos(f)}. \end{aligned} \tag{54}$$

Substituting all the terms back into Eq. (35) yields

$$\begin{cases} \tilde{x}'' - 2\,\tilde{y}' &= \tilde{\mathcal{W}}_{\tilde{x}}, \\ \tilde{y}'' + 2\,\tilde{x}' &= \tilde{\mathcal{W}}_{\tilde{y}}, \\ \tilde{z}'' &= \tilde{\mathcal{W}}_{\tilde{z}}. \end{cases} \tag{55}$$

where

$$\tilde{\mathcal{W}}_{\tilde{x}} = \left[\frac{1}{1 + e\, \cos f}\, \left(-\frac{1}{\tilde{\rho}^3} + 3\right)\right] \tilde{x}, \tag{56a}$$

$$\tilde{\mathcal{W}}_{\tilde{y}} = \left[\frac{1}{1 + e\, \cos f}\, \left(-\frac{1}{\tilde{\rho}^3}\right)\right] \tilde{y}, \tag{56b}$$

$$\tilde{\mathcal{W}}_{\tilde{z}} = \left[\frac{1}{1 + e\, \cos f}\, \left(-\frac{1}{\tilde{\rho}^3}\right) - 1\right] \tilde{z}. \tag{56c}$$

Note that the system Eq. (55) is equivalent to the elliptical Hill problem[9, 14, 16] as long as

$$\frac{\mathrm{d}(\,)}{\mathrm{d}\nu} = \frac{\mathrm{d}(\,)}{\mathrm{d}\theta} = \frac{\mathrm{d}(\,)}{\mathrm{d}f},$$

which is valid under the assumptions of the TBP (i.e., $J_2 = 0$, implying that the argument of periapsis stays constant).

References

[1] Spilker, L., "Cassini-Huygens'exploration of the Saturn system: 13 years of discovery," *Science*, Vol. 364, No. 6445, 2019, pp. 1046–1051. https://doi.org/10.1126/science.aat3760.

[2] Grasset, O., Dougherty, M., Coustenis, A., Bunce, E., Erd, C., Titov, D., Blanc, M., Coates, A., Drossart, P., Fletcher, L., et al.,

"JUpiter ICy moons Explorer (JUICE): An ESA mission to orbit Ganymede and to characterise the Jupiter system," *Planetary and Space Science*, Vol. 78, 2013, pp. 1–21.

[3] Boutonnet, A., and Schoenmaekers, J., "Jupiter tour of the JUpiter ICy moon Explorer," *Paper AAS 16-361 presented at the 2016 AAS/AIAA Space Flight Mechanics Meeting, Napa, CA*, AAS/AIAA, 2016.

[4] Campagnola, S., Buffington, B. B., Lam, T., Petropoulos, A. E., and Pellegrini, E., "Tour design techniques for the Europa Clipper mission," *Journal of Guidance, Control, and Dynamics*, Vol. 42, No. 12, 2019, pp. 2615–2626.

[5] Campagnola, S., Yam, C. H., Tsuda, Y., Ogawa, N., and Kawakatsu, Y., "Mission analysis for the Martian Moons Explorer (MMX) mission," *Acta Astronautica*, Vol. 146, 2018, pp. 409–417.

[6] Kuramoto, K., Kawakatsu, Y., Fujimoto, M., Araya, A., Barucci, M. A., Genda, H., Hirata, N., Ikeda, H., Imamura, T., Helbert, J., Kameda, S., Kobayashi, M., Kusano, H., Lawrence, D. J., Matsumoto, K., Michel, P., Miyamoto, H., Morota, T., Nakagawa, H., Nakamura, T., Ogawa, K., Otake, H., Ozaki, M., Russell, S., Sasaki, S., Sawada, H., Senshu, H., Tachibana, S., Terada, N., Ulamec, S., Usui, T., Wada, K., Watanabe, S.-i., and Yokota, S., "Martian moons exploration MMX: sample return mission to Phobos elucidating formation processes of habitable planets," *Earth, Planets and Space*, Vol. 74, No. 1, 2022, p. 12. https://doi.org/10.1186/s40623-021-01545-7, URL https://doi.org/10.1186/s40623-021-01545-7.

[7] Murchie, S. L., Thomas, P. C., Rivkin, A. S., and Chabot, N. L., "Phobos and Deimos," *Asteroids IV*, Vol. 4, 2015, p. 451.

[8] Scheeres, D. J., *Orbital motion in strongly perturbed environments: applications to asteroid, comet and planetary satellite orbiters*, Springer, 2016.

[9] Scheeres, D. J., Olikara, Z., Baresi, N., et al., "Dynamics in the Phobos environment," *Advances in Space Research*, Vol. 63, No. 1, 2019, pp. 476–495.

[10] Lara, M., and Juan, J. F. S., "Dynamic behavior of an orbiter around Europa," *Journal of Guidance, Control, and Dynamics*, Vol. 28, No. 2, 2005, pp. 291–297.

[11] Russell, R. P., "Global search for planar and three-dimensional periodic orbits near Europa," *The Journal of the Astronautical Sciences*, Vol. 54, No. 2, 2006, pp. 199–226.

[12] Russell, R. P., and Lara, M., "On the design of an Enceladus science orbit," *Acta Astronautica*, Vol. 65, No. 1-2, 2009, pp. 27–39.

[13] Wiesel, W. E., "Stable orbits about the Martian moons," *Journal of Guidance, Control, and Dynamics*, Vol. 16, No. 3, 1993, pp. 434–440.

[14] Voyatzis, G., Gkolias, I., and Varvoglis, H., "The dynamics of the elliptic Hill problem: periodic orbits and stability regions," *Celestial Mechanics and Dynamical Astronomy*, Vol. 113, No. 1, 2012, pp. 125–139.

[15] Ballouz, R. L., Baresi, N., Crites, S., Kawakatsu, Y., and Fujimoto, M., "Surface Refreshing of Martian moon Phobos by orbital eccentricity-driven grain motion," *Nature GeoScience*, 2019.

[16] Baresi, N., Dei Tos, D. A., Ikeda, H., and Kawakatsu, Y., "Trajectory Design and Maintenance of the Martian Moons eXploration Mission Around Phobos," *Journal of Guidance, Control, and Dynamics*, Vol. 44, No. 5, 2021, pp. 996–1007. https://doi.org/10.2514/1.g005041, URL https://doi.org/10.2514%2F1.g005041.

[17] Rambaux, N., Castillo-Rogez, J., Le Maistre, S., and Rosenblatt, P., "Rotational motion of Phobos," *Astronomy & Astrophysics*, Vol. 548, 2012, p. A14.

[18] Jezewski, D. J., "An analytic solution for the J2 perturbed equatorial orbit," *Celestial mechanics*, Vol. 30, No. 4, 1983, pp. 363–371. https://doi.org/10.1007/BF01375506, URL https://doi.org/10.1007/BF01375506.

[19] Martinuşi, V., and Gurfil, P., "Solutions and periodicity of satellite relative motion under even zonal harmonics perturbations," *Celestial Mechanics and Dynamical Astronomy*, Vol. 111, No. 4, 2011, pp. 387–414.

[20] Ascher, U. M., Mattheij, R. M., and Russell, R. D., *Numerical solution of boundary value problems for ordinary differential equations*, SIAM, 1995.

[21] Castella, E., and Jorba, À., "On the vertical families of two-dimensional tori near the triangular points of the bicircular problem," *Celestial Mechanics and Dynamical Astronomy*, Vol. 76, No. 1, 2000, pp. 35–54.

[22] Gómez, G., and Mondelo, J. M., "The dynamics around the collinear equilibrium points of the RTBP," *Physica D: Nonlinear Phenomena*, Vol. 157, No. 4, 2001, pp. 283–321.

[23] Olikara, Z. P., and Scheeres, D. J., "Numerical method for computing quasi-periodic orbits and their stability in the restricted three-body problem," *Advances in the Astronautical Sciences*, Vol. 145, No. 911-930, 2012, pp. 911–930.

[24] Baresi, N., Olikara, Z. P., and Scheeres, D. J., "Fully numerical methods for continuing families of quasi-periodic invariant tori in astrodynamics," *The Journal of the Astronautical Sciences*, Vol. 65, No. 2, 2018, pp. 157–182.

[25] Acton, C., "Ancillary data services of NASA's navigation and ancillary information facility," *Planetary and Space Science*, Vol. 44, No. 1, 1996, pp. 65–70.

[26] Acton, C., Bachman, N., Semenov, B., and Wright, E., "A look towards the future in the handling of space science mission geometry," *Planetary and Space Science*, Vol. 150, 2018, pp. 9–12.

[27] Harris, C. R., Millman, K. J., Van Der Walt, S. J., Gommers, R., Virtanen, P., Cournapeau, D., Wieser, E., Taylor, J., Berg, S., Smith, N. J., et al., "Array programming with NumPy," *Nature*, Vol. 585, No. 7825, 2020, pp. 357–362.

[28] Dang, Z., Luo, J., Shi, P., and Zhang, H., "General Characteristics of the Motion on J 2-Perturbed Equatorial Orbits," *Journal of Guidance, Control, and Dynamics*, Vol. 42, No. 10, 2019, pp. 2319–2324.

[29] Byrd, P. F., and Friedman, M. D., *Handbook of elliptic integrals for engineers and physicists*, Vol. 67, Springer, 2013.

[30] Hénon, M., *Generating families in the restricted three-body problem*, Vol. 52, Springer Science & Business Media, 1997.

[31] Jorba, A., and Villanueva, J., "On the persistence of lower dimensional invariant tori under quasi-periodic perturbations," *Journal of Nonlinear Science*, Vol. 7, No. 5, 1997, pp. 427–473.

[32] Olikara, Z. P., "Computation of quasi-periodic tori and heteroclinic connections in astrodynamics using collocation techniques," Ph.D. thesis, University of Colorado at Boulder, 2016.

[33] Broucke, R., "Stability of periodic orbits in the elliptic, restricted three-body problem." *AIAA journal*, Vol. 7, No. 6, 1969, pp. 1003–1009.

[34] Seydel, R., *Practical bifurcation and stability analysis*, Vol. 5, Springer Science Business Media, 2009.

[35] Broer, H. W., Huitema, G. B., and Sevryuk, M. B., *Quasi-periodic motions in families of dynamical systems: order amidst chaos*, Springer, 2009.

[36] Baresi, N., and Scheeres, D. J., "Quasi-periodic invariant tori of time-periodic dynamical systems: Applications to small body exploration," *Proceedings of the International Astronautical Congress*, 2016, pp. 9–26.

[37] McCarthy, B. P., and Howell, K. C., "Leveraging quasi-periodic orbits for trajectory design in cislunar space," *Astrodynamics*, Vol. 5, No. 2, 2021, pp. 139–165.